SENSITIVITY OF ROTOR AEROELASTIC PREDICTIONS WITH TWO-EQUATION TURBULENCE MODELS

Aaron Crawford, Georgia Institute of Technology, Atlanta, GA, USA
Pranav Sridhar, Georgia Institute of Technology, Atlanta, GA, USA
Marilyn J. Smith, Georgia Institute of Technology, Atlanta, GA, USA

Abstract

The capabilities of modeling complex rotor aeromechanics, principally via Computational Fluid Dynamics - Computational Structural Dynamics (CFD-CSD) coupling, have significantly improved with advancements in both computational hardware and software. Of particular interest is the accurate turbulence modeling for rotating blades in a variety of conditions, which remains the primary uncertainty in the prediction of rotorcraft aeromechanics. Recent collaborative investigations where different solvers and turbulence models are applied have yielded for some flight conditions dissimilar results while in other flight conditions, they produce comparable results. An investigation to further elucidate the root causes of this behavior has been undertaken with the series of two-equation models based on the Kok k-ω and Menter k-ω SST equations. The role that Delayed Detached Eddy Simulation (DDES) plays when added to these turbulence models is also of interest. These studies have been performed for both rotating and nonrotating configurations, applying a common solver, mesh, and time step. Both prescribed motion and aeroelastic applications have been examined for rotor flight conditions where the dichotomy between the two models was previously observed. Results indicate that the differences in the models occur when separated flows are present. Purely aerodynamic differences observed with rotor prescribed motion are compensated with structural dynamics when fully trimmed aeroelastic predictions are computed. The Kok k-ω turbulent eddy viscosity exhibited numerical growth that resulted in solver instability when large separation was encountered. The addition of the SST correction mitigated this growth, but DDES did not. Thus for these two turbulence models, if the same options (SST and/or DDES) are applied, differences can be attributed to the solvers, solver options, and/or meshes used in the simulation.

1. NOTATION

c	Chord, m
C_L/σ	Rotor lift coefficient
C_T	Rotor thrust coefficient, $T/(\rho\Omega\pi R^3)$
k	Turbulent kinetic energy, $(m/s)^2$
M_{tip}	Rotor tip Mach number
M^2C_n	Section normal force coefficient in the local airfoil frame
M^2C_m	Section pitching moment coefficient in the local airfoil frame
r	Local radial location, m
R	Rotor radius, m
u_j	Velocity vector components, m/s
U_∞	Freestream velocity, m/s
x_i	Cartesian direction components
x_{sep}	Normalized location of separation on chord, $(X_{location}/c)$
y^+	Nondimensional normal mesh spacing at wall
α_q	Rotor shaft angle, negative is forward tilt, deg
β_{1C}	Longitudinal flapping angle, deg
β_{1S}	Lateral flapping angle, deg
θ_0	collective pitch angle, deg
θ_{1C}	lateral cyclic pitch angle, deg
θ_{1S}	Longitudinal cyclic pitch angle, deg
ρ	Fluid density, kg/m^3
μ	Fluid viscosity, cP
μ_t	Turbulent eddy viscosity coefficient
σ	Rotor solidity, $N_b c/\pi R$
τ_{ij}	Reynolds stress tensor, $kg/(ms^{-2})$
ψ	Blade azimuth, deg
ω	Specific turbulent dissipation, $1/s$
Ω	Rotor angular velocity, rad/s

2. INTRODUCTION

The aeromechanics of rotors in flight are highly complex, defining the rotor performance, vibratory loads, and aeroacoustics. Solution of the unsteady Reynolds-averaged Navier-Stokes (uRANS) equations form the basis of high-fidelity computational fluid dynamics (CFD) solution that, when coupled with computational structural dynamics (CSD) methods hold the promise to accurately resolve these complex physics. Their numerical solution requires that the engineer make optimal decisions from a plethora of variables, such as turbulence closure, transition modeling, time step, and solver algorithm options. This is in addition to the development of a mesh where the governing equations are solved. These selections play an important role in the accuracy of the solution, in particular if unsteady flow separation and interactional aerodynamics are present.

The continuing enhancement and development of best practices of these aeroelastic (CFD-CSD) solvers to predict various aspects of rotor aeromechanics has been a focus of numerous studies and collaborative efforts over the past decade (including, but not limited to Refs. 1–6). Significant progress has been made, in particular due to the efforts of the UH-60A Airloads and the HART-II Workshops, described in review articles by Yeo and Ormiston (Refs. 7, 8) and Smith et al. (Ref. 9), respectively. Other efforts have focused on issues of dynamic stall (for a review, see Ref. 10) and transition (e.g., Refs. 11, 12). In addition to the multinational HART-II rotor tests (Ref. 13), which was primarily focused on aeroacoustics, the US UH-60A (Ref. 14) and the French 7A rotor (Ref. 15) wind tunnel campaigns with their significant instrumentation provide high-quality wind tunnel tests to support computational validations of rotors in forward flight.

In one of these collaborations, a joint effort between the United States and France, the four-bladed fully-articulated 7A and UH-60A rotors were evaluated computationally to assess the capabilities of high-fidelity uRANS CFD and CFD-CSD solvers to predict complex separation phenomena and add insights into the underlying physics driving these phenomena (Refs. 16, 17). The collaborators applied the structured Navier-Stokes code elsA (Ref. 18), using the Kok k-ω with SST correction (Refs. 19, 20) with comparable (though not exact) meshes and simulation options as the structured Navier-Stokes code OVERFLOW (Ref. 21), applying the Menter k-ω SST turbulence model with DDES (Ref. 20). While in some cases the results were almost identical, in other instances they varied significantly from one another. Further, computational correlations with wind tunnel results were not consistent, where one computational prediction was observed to be more accurate than the other, but less accurate in other flight conditions. While these studies allowed each collaborating partner to assess and compare their state-of-the-art processes independently, the role of the different turbulence modeling approaches and their significance in defining the best practices of rotor aeromechanics predictions remains unresolved.

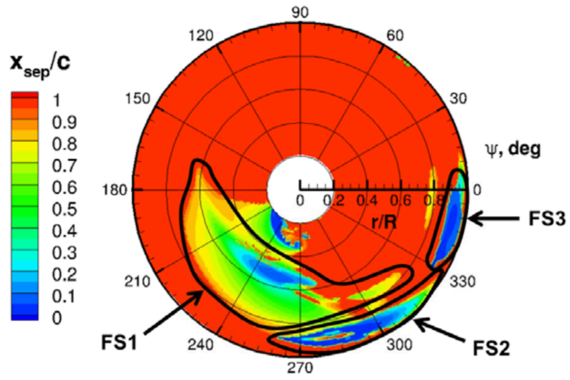

(a) Test Point 293 moderate dynamic stall occurring at μ =0.3, θ_0=8.4°, and M_{tip} =0.646

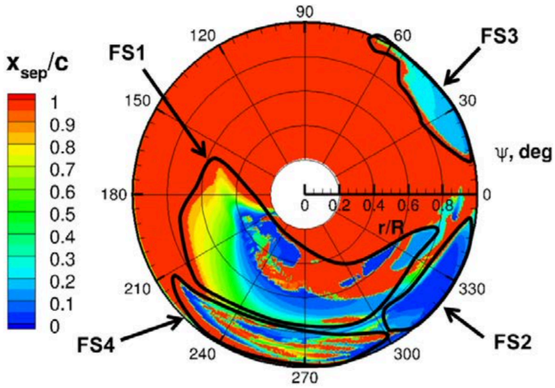

(b) Test Point 405 deep dynamic stall occurring at μ =0.42, θ_0=12.6°, and M_{tip} =0.616

Figure 1: Regions of separated flows on the 7A rotor, as defined by Richez (Ref. 22).

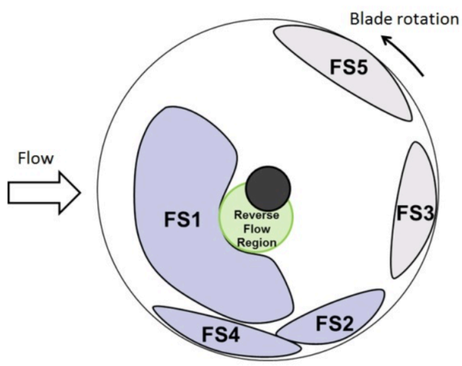

Figure 2: Schematic of rotor separation regions (Ref. 16).

The flight conditions where the most prominent differences in predictions were observed occurred in the presence of separated flows, observed for both for the 7A and UH-60A rotors. Richez (Ref. 22) has identified multiple regions of separated flows for differing flight conditions for the 7A rotor, as illustrated in Fig. 1. The regions of flow separation is identified by the extent of separation, where $x_{sep} = 1.0$ denotes fully attached flow and $x_{sep} = 0.0$ is fully separated flow. These rotor maps were extended and generalized by Grubb et al. (Ref. 16) when additional approaches (solvers, turbulence models, transition) were explored, defined in Fig. 2. These distinct regions of separation have been related to the causal physics, and similar regions were identified under comparable conditions.

Using the schematic in Fig. 2 as a reference, the causal physics can be elucidated. These regions vary in extent, magnitude, and even their presence, depending on the flight conditions for the 7A and when extended to other rotors. FS1 denotes the flow separation emanating from increasing trailing edge separation, located primarily on the retreating side of the rotor. FS2, occurs from a more abrupt leading edge separation. These have both been identified as emanating from blade vortex interactions (BVI), where FS1 tends to occur from less severe BVI, while FS2 results from strong, prolonged oblique rotor-vortex interchanges. The influence of BVI on rotor separation and dynamic stall has been additionally explored by Castells et al. (Ref. 23) and Grubb et al. (Ref. 6).

FS3 was not observed in experiments, but appeared only in computational results on the outer blade in the latter portion of the fourth quadrant (near ψ =360°). The cause of this region was explored further (Ref. 16), and it was determined to be an artifact of the CFD-CSD coupling. This region can be characterized by a high angle of attack which can verge on the edge of rotor stall. Thus, the comprehensive code coupling appears to drive this region, as a collective trim variation of a degree or less determines the stall characteristics. This region may also be influenced by the significant wake created by the fuselage and rotor. The blade elasticity (torsion) controls the extent of the FS3 region. The most significantly variability among approaches was observed in the definition and behavior of this region.

At higher loading conditions, a new region, FS4, can be defined. This separation region, which can result in dynamic stall, is characterized by the rotor kinematics rather than BVI. Thus, this region is the embodiment of the definition of classic dynamic stall. Likewise, the presence of the FS3 and FS4 regions typify the performance limitation defined in the literature introduced by dynamic stall.

Under some conditions observed for the 7A and UH-60A rotors, a fifth flow separation region, FS5, in the first rotor quadrant (advancing side) was present from shock-boundary layer interaction near the rotor tip, typically without inducing a dynamic stall event (Refs. 16, 17). For the 7A rotor, Grubb et al. (Ref. 16) noted that uRANS predictions were more accurate on the advancing rotor disk, but the addition of Delayed Detached Eddy Simulation (DDES) enhanced airloads predictions on the retreating side of the rotor disk. Overall the one-equation Spalart-Allmaras turbulence model was less accurate than the two-equation counterparts evaluated, and thus only two-equation models were carried forward in the UH-60A studies (Ref. 17).

To explore the uncertainty between the two two-equation turbulence models, the Kok k-ω turbulence model has been implemented into OVERFLOW to permit direct comparison of the turbulence models under identical operating conditions. The role of Delayed Detached Eddy Simulation (DDES) is separated from the underlying unsteady uRANS turbulence closure. The aerodynamic influence is isolated using prescribed motion first, followed by the full aeroelastic computations to identify their role in CFD-CSD coupling.

3. TURBULENCE MODEL GOVERNING EQUATIONS

3.1. Wilcox k-ω Turbulence Model

The original two-equation k-ω of Wilcox (Refs. 24, 25) is defined as:

$$\begin{aligned} \frac{D\rho k}{Dt} &= \frac{\partial(\rho k)}{\partial t} + \frac{\partial(\rho k u_j)}{\partial x_j} = \\ &\tau_{ij}\frac{\partial u_i}{\partial x_j} - \beta^*\rho\omega k + \frac{\partial}{\partial x_j}\left((\mu + \sigma^*\mu_t)\frac{\partial k}{\partial x_j}\right) \end{aligned} \tag{1}$$

$$\begin{aligned} \frac{D\rho\omega}{Dt} &= \frac{\partial(\rho\omega)}{\partial t} + \frac{\partial(\rho\omega u_j)}{\partial x_j} = \\ &\frac{\gamma\omega}{k}\tau_{ij}\frac{\partial u_i}{\partial x_j} - \beta\rho\omega^2 + \frac{\partial}{\partial x_j}\left((\mu + \sigma\mu_t)\frac{\partial\omega}{\partial x_j}\right) \end{aligned} \tag{2}$$

In Equations 1-2, the Reynolds stress tensors τ_{ij} (Ref. 24) have the form

$$\tau_{ij} = 2\mu_t\left(S_{ij} - \frac{1}{3}\frac{\partial u_k}{\partial x_k}\delta_{ij}\right) - \frac{2}{3}\rho k\delta_{ij} \tag{3}$$

$$S_{ij} = \frac{1}{2}\left(\frac{\partial u_j}{\partial x_i} + \frac{\partial u_j}{\partial x_i}\right) \tag{4}$$

In the Wilcox formulation, the turbulent mixing energy and specific dissipation rate are needed to define the eddy viscosity coefficient μ_t

(5) $$\mu_t = \gamma^* \frac{\rho k}{\omega}$$

The turbulence closure coefficients in the Wilcox model applied in the study are

$$\beta = \frac{3}{40} \quad \beta^* = \frac{9}{100} \quad \gamma = \frac{5}{9}$$

$$\gamma^* = 1 \quad \sigma = \frac{1}{2} \quad \sigma^* = \frac{1}{2}$$

3.2. Menter k-ω SST Turbulence Model

The Menter k-ω SST model sought to leverage the robustness and accuracy of the Wilcox k-ω model in the near wall region and the freestream independence of the k-ϵ model in the outer part of the boundary layer, as described in Menter (Ref. 20). This approach required transforming the k-ϵ model into a k-ω formation, which introduces an additional cross-diffusion term that appears in the ω equation. The Menter k-ω SST model multiplies the original Wilcox k-ω model by a function F_1 and the modified k-ϵ model by $(1 - F_1)$, and the sum of the two models is then applied. The function F_1 is a blending function which equals one in the near wall region, activating the Wilcox k-ω model, and should equal zero in the wake region of the boundary, triggering the modified k-ϵ model. This formulation results in the following equation set known as the Menter k-ω SST model, defined in Menter's 1994 publication (Ref. 20):

(6) $$\frac{D\rho k}{Dt} = \frac{\partial (\rho k)}{\partial t} + \frac{\partial (\rho k u_j)}{\partial x_j} = \tau_{ij}\frac{\partial u_i}{\partial x_j} - \beta^* \rho \omega k + \frac{\partial}{\partial x_j}\left((\mu + \sigma_k \mu_t) \frac{\partial k}{\partial x_k} \right)$$

(7) $$\frac{D\rho \omega}{Dt} = \frac{\partial (\rho \omega)}{\partial t} + \frac{\partial (\rho \omega u_j)}{\partial x_j} = \frac{\gamma}{\nu_t}\tau_{ij}\frac{\partial u_i}{\partial x_j} - \beta \rho \omega^2 + \frac{\partial}{\partial x_j}\left((\mu + \sigma_\omega \mu_t) \frac{\partial \omega}{\partial x_j} \right) + 2(1 - F_1)\rho\sigma_{\omega 2}\frac{1}{\omega}\frac{\partial k}{\partial x_j}\frac{\partial \omega}{\partial x_j}$$

The blending function F_1 is

(8) $$F_1 = \tanh\left(arg_1^4\right)$$

(9) $$arg_1 = \min\left(\max\left(\frac{\sqrt{k}}{0.09\omega y}, \frac{500\nu}{y^2\omega} \right), \frac{4\rho\sigma_{\omega 2} k}{CD_{k\omega} y^2} \right)$$

(10) $$CD_{k\omega} = \max\left(2\rho\sigma_{\omega 2}\frac{1}{\omega}\frac{\partial k}{\partial x_j}\frac{\partial \omega}{\partial x_j}, 10^{-20} \right)$$

The eddy viscosity coefficient in the Menter k-ω SST model

(11) $$\mu_t = \frac{a_1 \rho k}{\max(a_1\omega, \Omega F_2)}$$

also uses a blending function F_2, where Ω is the absolute value of the vorticity. The blending function F_2 is

(12) $$F_2 = \tanh\left(arg_2^2\right)$$

(13) $$arg_2 = \max\left(\frac{\sqrt{k}}{0.09\omega y}, \frac{500\nu}{y^2\omega} \right)$$

Computing the turbulence closure constants for the Menter k-ω SST model requires computing a weighted sum of the Wilcox and k-ϵ turbulence closures. An arbitrary turbulence closure parameter, ϕ, is computed using ϕ_1, the closure quantity from the Wilcox model, and ϕ_2, the turbulence closure quantity from the k-ϵ model:

(14) $$\phi = F_1\phi_1 + (1 - F_1)\phi_2$$

The turbulence closures from the Wilcox model are modified to obtain the Shear-Stress Transport (SST)

$$\sigma_{k1} = 0.85 \quad \sigma_{\omega 1} = 0.5 \quad \beta_1 = 0.0750 \quad a_1 = 0.31$$

$$\beta^* = 0.09 \quad \kappa = 0.41 \quad \gamma_1 = \frac{\beta_1}{\beta^*} - \frac{\sigma_{\omega 1}\kappa^2}{\sqrt{\beta^*}}$$

The turbulence closures from the k-ϵ model, applied in this analysis, are

$$\sigma_{k2} = 1.0 \quad \sigma_{\omega 2} = 0.856 \quad \beta_2 = 0.0828$$

$$\beta^* = 0.09 \quad \kappa = 0.41 \quad \gamma_2 = \frac{\beta_2}{\beta^*} - \frac{\sigma_{\omega 2}\kappa^2}{\sqrt{\beta^*}}$$

OVERFLOW uses an updated version of the Menter SST model (Refs. 21, 26) in its implementation of the turbulence model, which has only a few minor differences to the original 1994 Menter SST model. These updates are also detailed in the NASA Turbulence Modeling Resource (Ref. 27).

3.3. Kok k-ω Turbulence Model

A limitation of the Menter k-ω SST model is that the wall distance is needed to compute the blending function. Wilcox later proposed including the cross-diffusion term without a blending function which would switch off when in the near-wall region to not affect the behavior of the k-ω model (Ref. 28). Kok proved that the model coefficients used by Wilcox for his model did not resolve the freestream dependency and proposed a difference set of turbulence closure constants to resolve this issue (Ref. 19). The Kok k-ω model from his 2000 work is:

$$\frac{D\rho k}{Dt} = \frac{\partial(\rho k)}{\partial t} + \frac{\partial(\rho k u_j)}{\partial x_j} = P_k - \beta^* \rho \omega k + \frac{\partial}{\partial x_j}\left((\mu + \sigma_k \mu_t)\frac{\partial k}{\partial x_j}\right) \tag{15}$$

$$\frac{D\rho \omega}{Dt} = \frac{\partial(\rho \omega)}{\partial t} + \frac{\partial(\rho \omega u_j)}{\partial x_j} = P_\omega - \beta \rho \omega^2 + \frac{\partial}{\partial x_j}\left((\mu + \sigma_\omega \mu_t)\frac{\partial \omega}{\partial x_j}\right) + C_D \tag{16}$$

In Equations 15 and 16, the production terms P_k and P_ω and cross-diffusion term C_D take the following forms

$$P_k = \tau_{ij}\frac{\partial u_j}{\partial x_i} \tag{17}$$

$$P_\omega = \alpha_\omega \omega \frac{P_k}{k} \tag{18}$$

$$C_D = \sigma_d \frac{\rho}{\omega} \max\left(\frac{\partial k}{\partial x_i}\frac{\partial \omega}{\partial x_i}, 0\right) \tag{19}$$

The Kok k-ω model defines the eddy viscosity coefficient using the original Wilcox k-ω model given in Equation 5, where $\gamma^* = 1$. The Kok k-ω model has six turbulence closure coefficients:

$$\beta^* = 0.09 \quad \frac{\beta^*}{\beta} = \tfrac{6}{5} \quad \kappa = 0.41$$
$$\alpha_\omega = \frac{\beta}{\beta^*} - \sigma_\omega \frac{\kappa^2}{\sqrt{\beta^*}}$$
$$\sigma_\omega = 0.5 \quad \sigma_k = \frac{2}{3} \quad \sigma_d = 0.5$$

3.4. Kok k-ω Model with SST Correction

The origin of the questions leading to the analysis performed in this paper applied the elsA solver. The implementation of Kok k-ω model in elsA uses the 1994 Kok k-ω model with the SST correction (Refs. 19, 20). This formulation uses the turbulence equations and turbulence closures from the Kok model with the definition of the eddy viscosity coefficient from the SST model previously defined in Equations 11 through 13.

3.5. Delayed Detached Eddy Simulation (DDES)

This study also examined the influence of applying the DDES approach for the three-dimensional rotating cases. The existing DDES implementation in OVERFLOW is applied here with the Menter k-ω SST and Kok k-ω models (Ref. 29).

4. TECHNICAL APPROACH

To test the influence of two-equation turbulence models, the different options were all implemented into a single solver, if they were not already present. For consistency, all simulations were resolved using identical meshes and numerical options.

The solver selected for this study is OVERFLOW (Ref. 30), a NASA-developed structured, overset methodology that is a standard for engineering analysis in both the fixed-wing and rotorcraft communities. OVERFLOW includes high-order spatial-differencing schemes to accurately preserve vorticity and pressure fluctuations, important for aeromechanics. Flexibility to model complex geometries is achieved through its ability to overset meshes. Its rotorcraft capabilities are extended via coupling with other industry standard analysis tools, such as RCAS (Ref. 31) and ANOPP2 (Ref. 32) for aeroelastic and aeroacoustic predictions, respectively. OVERFLOW is also a near-body solver in the DoD HPCMP CREATE™-AV Helios suite (Ref. 33), extending its capabilities even further.

The Menter k-ω SST turbulence model, along with the DDES capability was extant in OVERFLOW prior to this study. The Kok k-ω turbulence model, along with the SST correction and DDES capability were added to the solver for this study.

To verify the functionally of the Kok k-ω turbulence model and to further understand its comparability with the Menter k-ω model, two-dimensional airfoil cases were analyzed, with a brief summary of the results included herein. In addition, a non-rotating wing was examined. The Kok k-ω SST and Kok k-ω DDES variations were not evaluated on the non-rotating cases.

A rotor including both prescribed and trimmed aeroelastic simulations were examined to differentiate pure aerodynamic behavior and to understand the impact of an aeroelastic analysis. Two rotor conditions, applying various versions of the Kok and Menter two-equation turbulence models were evaluated.

4.1. Two-Dimensional Airfoil Validation

After implementation of the Kok k-ω model, the verification and validation of its base functionality was required. A NACA 0012 and a NACA 4412 were examined, utilizing well-documented experimental data (Refs. 34, 35). A C type structured mesh was generated with a mesh 249 points in the streamwise and 59 points in the normal directions. The normal mesh ensured the standard $y+$ of 1 was maintained for accurate boundary layer predictions. The evaluation was performed at a freestream Mach number of 0.15 for four angles of attack from 0° to 16° in approximate intervals of 4°, performed in accordance with the NASA turbulence modeling resource (Ref. 27). Integrated lift and drag, as well as the C_p distribution over the airfoil, were compared.

4.2. Three-Dimensional Finite Wing

A three-dimensional wing was evaluated to identify aerodynamic predictive differences between the Menter k-ω SST and Kok k-ω models before adding the complexity of rotation. Included as a test case in the OVERFLOW package is the three-dimensional NASA NLF(2)-0415 wing, hereafter referred to as the Sickle wing (Refs. 21, 36). In this case, the wing root is adjacent to one of the vertical faces of the domain, and the wing near-body structured mesh consists of two blocks: the main wing and the wing tip cap. The meshes were generated using the Chimera grid tools, with a total point count of roughly 17.56 million near-body points and 400,000 off-body points, with the same meshes used for both the Menter k-ω SST and Kok k-ω models (Ref. 37). The near-body mesh can be seen in Figure 3. The comparisons for the Sickle wing are done at a Mach number of 0.16 for angles of attack of -2.6°, 9°, and 14°, and were run for 10,000 iterations with 40 subiterations. Integrated lift and drag, as well as the C_p distribution at various spanwise stations are compared for the Kok k-ω and Menter k-ω SST models.

4.3. Aeroelastic Rotor with Prescribed Motion

This rotor evaluation focused on identifying the aerodynamic differences between the different models, without aeroelastic effects. The computational analysis mirrors experimental tests on the 7A rotor performed by ONERA (Ref. 15). The rotor was examined experimentally in high-speed and high-thrust conditions that induce dynamic stall using a variety of mechanisms (Refs. 16, 17). Two cases were selected that result in moderate dynamic stall (Test Point 293) and deep dynamic stall (Test Point 405) (Ref. 16).

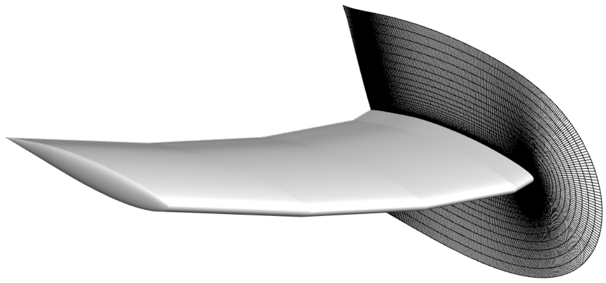

Figure 3: Sickle wing surface with near-body normal mesh.

The computational configuration included the nacelle and rotor blades, represented via structured near-body meshes. The meshes were provided and adapted from previous efforts (Ref. 16). The nacelle is modeled by a single block, while each rotor blade consists of three structured blocks, one each for the blade root, main blade, and blade tip. The blade mesh is constructed for only one blade and then mirrored about the center of rotation to place the remaining three blades. The near-body mesh extends 150mm ($\approx$1.1c) from the blade surface and 250mm ($\approx$1.8c) from the nacelle surface. A constant fine spacing refinement region is centered around the rotor rotational axis and extends approximately 1.5R in both streamwise and spanwise directions. It extends 1.5R in negative blade normal direction and approximately 0.5R in the positive blade normal direction. This region has a constant spacing of less than 0.1c. The far-field mesh extends over 20 rotor radii in every direction. Further mesh details are provided in Tab. 1 and is illustrated in Fig. 4. Simulations were performed for five rotor revolutions with quarter degrees rotation per timestep. Sixty subiterations at each time step, providing a minimum convergence of one order of magnitude.

To evaluate the differences in the turbulence models, prescribed motion computed from previous computational simulations (Ref. 16) was applied. This prescribed motion dictates the blade deformations over the entire rotor blade at each azimuthal position. This setup mimics the effects of aeroelasticity that are found on a traditional helicopter rotor, but permits a direct comparison of the aerodynamics by removing the influence of the CFD/CSD coupling process.

Characteristic	Quantity
Wall Spacing	0.0017(Nacelle) 0.000947(Blade)
$y+$	1
Normal Points	104
Leading Edge Refinement	0.161 (0.22 c%)
Trailing Edge Refinement	0.0386 (0.054 c%)
Total Near Body Points	16.2 Million
Total Off-Body Points	164 Million (SAMCart) 199 Million (OVERFLOW)

Table 1: 7A Rotor Mesh Statistics.

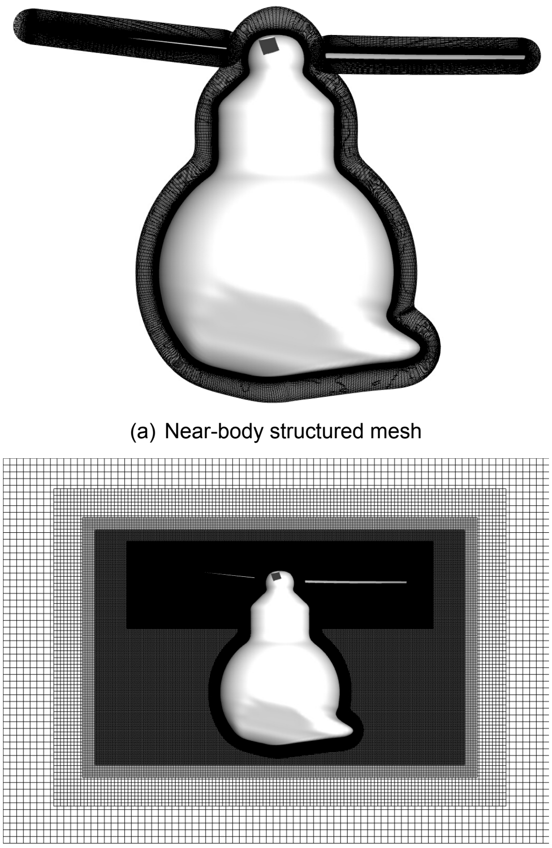

(a) Near-body structured mesh

(b) Off-body Cartesian mesh

Figure 4: Computational meshes for the 7A rotor.

4.4. Trimmed Aeroelastic Rotor

The aeroelastic (CFD-CSD) ONERA 7A simulations were resolved within the CREATE-AV Helios (Refs. 33, 38) framework which couples OVERFLOW with Rotorcraft Comprehensive Analysis System (RCAS) (Ref. 38). Helios uses a dual mesh paradigm, using a Cartesian off-body mesh solver, SAMCart (Ref. 33). The SAMCart solver generates the off-body Cartesian mesh for the coupled cases, using a fifth order central differencing in space and second order backwards differencing in time (Refs. 33, 39, 40)

The aerodynamic loads from the CFD near-body solver are transferred to RCAS to compute the blade deformations and determine the target trim state based on user inputs. The blade deformation and trim state are then transferred back to the aerodynamic solver where the rotor blade is deformed, and the collective is modified to reflect the new trim condition. The aeroelastic analyses employs loose CFD-CSD coupling first introduced by Potsdam et al. (Ref. 41) and previously applied to the 7A rotor (Ref. 4). The CFD-CSD exchange occurs every 90 degrees azimuth after the first rotor revolution, where the exchange occurs every 180 degrees.

The aeroelastic rotor flight conditions and meshes applied in this portion of the analysis replicate those performed by Grubb et al. (Ref. 16). To observe how the turbulence models behave in rotor conditions where differences were previously observed (Refs. 16, 17), two conditions that include moderate and deep dynamic stall (DS) events were examined, per Tab. 2.

	Moderate DS	Deep DS
α_q	-6.7	-11.65
θ_0	8.4	12.6
θ_{1c}	3.16	3.7
θ_{1S}	-3.51	-5.9
M_{tip}	0.646	0.616
μ	0.3	0.42
C_L/σ	0.100	0.095
C_X/σ	0.0046	0.0085
Flapping Law	$\beta_{1S}=0$ $\beta_{1C}+\theta_{1S}=0$	$\beta_{1S}=0$ $\beta_{1C}+\theta_{1S}=0$

Table 2: Rotor conditions for the coupled CFD-CSD 7A cases

5. RESULTS

5.1. Two-Dimensional Airfoil Validation

As previously introduced, the implementation of the Kok k-ω model was validated for the NACA 0012 and NACA 4412 test cases documented in the NASA Turbulence Modeling Resource (Ref. 27). The NACA 0012 test case was performed for five angles of attack in the attached and near-stall regimes. Figure 5(a) illustrates the variation of the lift coefficient with the angle of attack, where the predicted lift coefficient from the Kok k-ω and Menter k-ω SST models track well (within 0.02) with experimental data and one another. The difference between the two models increases with angle of attack as a second-order polynomial. At larger angles of attack, the Kok k-ω model predicts the lift coefficient closer to the Ladson experimental data compared to the Menter k-ω SST model, at ~2% and ~5%, respectively. The drag polar predictions in Fig. 5(b) indicate that both turbulence models increasingly over predict the drag coefficient as angle of attack increases. The differences in the two models is relatively constant until the effects of the incipient stall are apparent. As stall effects become apparent, the differences between the two models and their ability to predict the drag increase substantially. As previously noted for the lift, the Kok k-ω model is closer to the experimental data than the Menter k-ω SST model. While there are not experimental pitching moment data, the differences between the two turbulence model pitching moment predictions are similar to those observed for the drag.

For further insight, the pressure coefficient distribution at an angle of attack of 10° was compared in Fig. 5(c) including experiment (Ref. 34). The pressure coefficient for the Kok k-ω and Menter k-ω SST turbulence models are coincident almost entirely, confirming the agreement between the two turbulence models. A very small difference between the two models makes an appearance over the last 10% of the chord. As the differences increase above this angle of attack with the onset of stall, the model behavior at the trailing edge indicates that the differences in the two models is likely related to flow separation.

5.2. Three-Dimensional Finite Wing

The three-dimensional non-rotating wing was evaluated primarily via the distribution of the pressure coefficient on the surface, which provides insight into the behavior of the two turbulence models. These evaluations, not shown due to paper length, indicated virtually identical pressure coefficients at all span stations for the low angle of attack analyzed (-2.6°). For the higher angles of attack evaluated (9° and 14°), the only noticeable difference in pressure coefficient ($\approx$ 5%) occurs at the wing finite tip, y/L = 1.

Integrated aerodynamic quantities confirmed the pressure coefficient observations. Differences between lift, drag and pitching moment coefficients for the Mentor k-ω SST and Kok k-ω models were confined primarily to the third decimal place for all three angles of attack analyzed. For values not close to zero where percentages are disproportionately large, differences were typically within 2%–3%, verifying the implementation of the Kok k-ω in OVERFLOW and

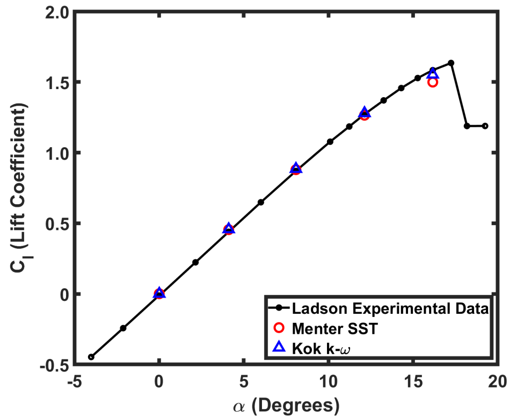

(a) Sectional lift coefficient (C_l) variation with angle of attack (α) data

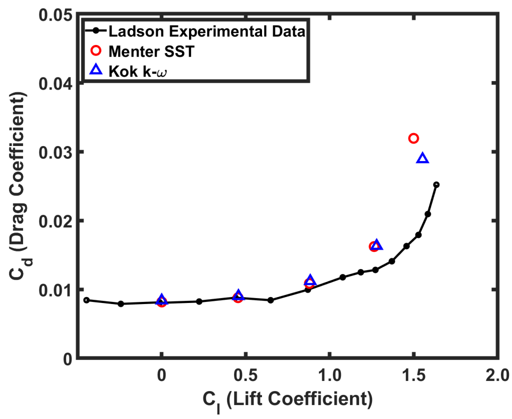

(b) Drag polar

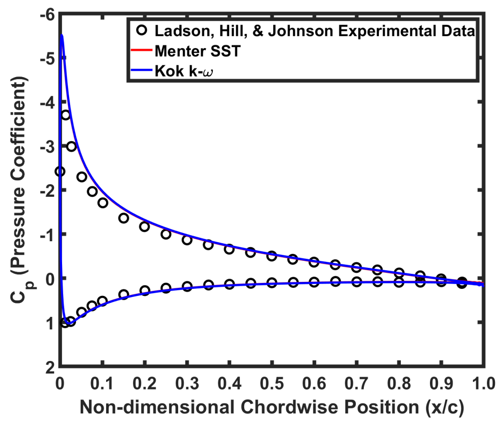

(c) Pressure coefficient distribution at 10° angle of attack

Figure 5: Comparison of NACA 0012 airfoil simulation results using the Menter k-ω SST and Kok k-ω turbulence models and experimental data (Ref. 35)

confirming comparable behavior for attached flows.

5.3. Aeroelastic Rotor with Prescribed Motion

The simulations with prescribed aeroelastic motion were evaluated after five rotor revolutions (solution is periodic) of the 7A rotor using the integrated forces and moments, as well as the separation location computed during the final revolution. For the moderate stall case, turbulence models evaluated were Menter k-ω SST, Menter k-ω SST DDES, Kok k-ω, Kok k-ω DDES, and Kok k-ω with SST correction models. For the deep stall case, the Kok k-ω and Kok k-ω DDES simulations exhibited some issues with convergence and are thus not included. The sectional normal force and pitching moment coefficients have been extracted at various radial stations where experimental data are available (Ref. 15).

5.3.1. Moderate Dynamic Stall

Figures 6 and 7 render the normal force and pitching moments for the different turbulence models after convergence. It is evident, given the superposition of the predictions that, over most of the rotor revolution, the turbulence models exhibit almost identical behavior for both the normal force and pitching moment coefficients. The largest differences between the turbulence models are consistently observed over the retreating section of the rotor disk at outboard radial stations, extending into the early portion of the first quadrant as the two methodologies synchronize after the flow reattaches. The largest excursions are observed in solutions from the Kok k-ω with DDES simulations. Inspection of this behavior appears to be due to a large growth in the turbulent viscosity, μ_t, of the Kok k-ω model, but further analysis is underway.

From approximately 270° to 10°, the prescribed motion defines the control angles and the blade torsion at 12°–14°, initiating separated flow conditions on the outer half of the rotor blade. Correspondingly, between 270° and 45°, some variation between the models occur. The influence of the SST correction applied to the original Kok k-ω model, moves the predictions closer to that of the Menter k-ω SST, outside of dynamic stall events. The addition of the SST correction, appears to constrain the large growth of the Kok k-ω model's μ_t previously noted. This is most readily observed from 360°–340° at r/R = 91.5% for pitching moment and r/R = 82.5% for the normal coefficient. This location corresponds to the FS3 region that was attributed primarily to the coupling and susceptible to rotor stall conditions, indicating that the aerodynamic model can also contribute to the sensitivity of the computations.

There are also some differences during dynamic stall, which are exacerbated as the rotor tip is approached. The normal force stall that occurs at approximately 280° is predicted comparably by all models at r/R = 70% (Fig. 6b)), but are significantly (approximately 15%) different in magnitude with a minor phase difference (Kok leads Menter by 2°) by r/R = 91.5% (Fig. 6d)). Notably DDES has minimal impact on the prediction of the normal force dynamic stall event.

A moment stall leads the force stall for this condition, occurring just prior to 270° at r/R = 50%, shifting aft to ~280° by r/R = 91.5% (Fig. 7). As noted by Grubb et al.(Ref. 16), the variation between turbulence models was greater for pitching moment than normal force, and that is observed here, even when the CFD-CSD coupling is not part of the simulations. Unlike the Menter models, where DDES had little influence on the predictions, the Kok k-ω DDES model did modify the original model predictions. However, the differences in between the DDES and uRANS Kok models were inconsistent. There was a large deviation during the stall event at r/R = 50% (Fig. 7a)), but for no other radial stations. Differences were observed for the three stations at r/R = 81.5% and outboard, after the stall event between approximately 320° – 360°.

Integrating the sectional loads over the blade (Tab. 3), the rotor lift coefficient (C_L/σ) confirms the observations of the radial stations. The Menter k-ω SST and Kok k-ω SST models are only 0.59% apart. The addition of DDES is also confirmed to be negligible with a difference of 0.04% and 0.01% for the Menter and Kok models with and without DDES. However, the implementation of the SST correction with the Kok k-ω model indicates a significant difference, as discussed previously for the rotor loads. The difference between the Menter and Kok rotor lift coefficient decreases from 0.59% to 0.001%.

Rotor maps of the separation locations were compared in Fig. 8. It is evident in comparing the uRANS (with SST) (Fig. 8(a)) and DDES (Fig. 8(b)) implementations of the Menter model that the prediction separation is almost identical. The Kok model with SST Fig. 8(e)) is also comparable to the Menter model. Comparing the three Kok models, the inconsistent deviations observed by the DDES (Fig. 8(d)) model are evident in the intersecting region of FS1-FS2-FS4 and difference in areas of FS3. The original Kok model has a greater extent of FS5 than its SST and DDES counterparts, as well as a slower recovery from the FS1 region.

For this 7A rotor flight condition, the Menter and Kok models with the SST corrections are almost identical. DDES corrections do not improve the rotor airloads predictions with the applied numerical options and given mesh.

Turbulence Model	C_L/σ
Menter SST	0.10363
Menter SST DDES	0.10367
Kok k-ω	0.10424
Kok k-ω SST	0.10346
Kok k-ω DDES	0.10328

Table 3: Rotor lift coefficient (C_L/σ) computed using different turbulence models for moderate dynamic stall case with the prescribed aeroelastic motion.

5.3.2. Deep Dynamic Stall

The same metrics were examined for the deep dynamic stall case using prescribed motion. Again, the prescribed motion was extracted from Grubb et al. (Ref. 16). Given the influence of the SST correction on the Kok k-ω model when compared to the Menter k-ω SST model, only the Kok k-ω SST model was evaluated. In addition, the inconsistencies observed in the Kok k-ω and Kok k-ω DDES model translated to stability issues for the deep stall case. This is under further investigation.

Figures 9 and 10 depict the azimuthal variation in the sectional normal force and pitching moment coefficients at various radial locations. Once again, the models predict the same force and pitching moment on the advancing rotor disk. On the retreating rotor disk, differences appear once angles at and beyond the onset of stall are introduced. These differences are much more significant than those observed for the moderate dynamic stall case. For this deep stall case, the rotor blade angles exceeds 12° between azimuthal angles of 190° – 50°, exceeding 20° between azimuthal angles of 260° – 350°, with a maximum value of 22° around 310°. These angles are consistent across the entire outer half of the blade radius.

Differences in the normal force are observed between the Menter k-ω SST model and the Kok k-ω SST model in the region of Ψ=270° – 360° with the most prominent differences at r/R=70% (Fig. 9(b)) and r/R=91.5% (Fig. 9(d)). No clear trend between the two models can be ascertained as larger variations are predicted by each model at different locations. This is borne out by the computation of the rotor lift coefficient (C_L/σ), which yielded differences between the Kok and Menter models of less than 1%. For the Menter k-ω SST model, the addition of DDES is observed to be insignificant as with the moderate stall case.

For the pitching moments (Fig. 10), overall similar behavior is observed with a few caveats. The Kok k-ω SST model introduces moment stalls that are significantly stronger than those predicted by the Menter k-ω SST model. This behavior is observed across all radial locations, though the differences in magnitudes are exacerbated at the outer radial stations. Both the Menter k-ω SST DDES and Kok k-ω SST models predict an additional moment stall at 270° at r/R=91.5% that is not observed in experiment or Menter k-ω SST. The Kok k-ω SST model also does not predict the moment recovery for r/R=97.5% between 280°–360°. The difference in this area was also observed for the moderate dynamic stall case, albeit without the large excursions noted here.

Figure 11 maps the separation locations for the different models over the rotor disk. If these are mapped to the separation regions defined by Fig. 2, the different flow separation (FS) zones are not longer distinct as show in the schematic and observed for the moderate dynamic stall case (Fig. 8) as leading edge separation dominates the outer blade radius over most of the rotor disk.

Within these maps, subtle differences are found between all simulations, with slight deviations seen in the size and location of separation regions. The dominant regions of separation are effectively the same. The size and extent of FS5 region (outboard most region of 30°–90°) is the most obvious difference between the Kok and Menter models.

5.4. Trimmed Aeroelastic Rotor

The results from the prior section (Sect. 5.3.) was instrumental in determining the actual aerodynamic differences for the 7A rotor without the influence of an external CSD solver. However, the solutions in the prior section are not indicative of the actual predictive capabilities of the turbulence models for an aeroelastic rotor as the CFD and CSD codes interactive to provide an accurate solution. Therefore, the final analyses were performed for OVERFLOW+RCAS to elucidate how the aerodynamic differences in these models impact the aeroelastic rotor predictions.

Because of issues encountered in the stability of the Kok k-ω model with DDES (the SST correction has not yet been integrated with DDES), only the moderate dynamic stall case was examined. However, this case provides excellent insight into the question posed herein.

CFD-CSD coupled simulations were performed via the comprehensive solver RCAS, where the coupling parameters matched those previously by Grubb et al. (Ref. 16). The evaluations were performed for the baseline uRANS Menter k-ω SST and Kok k-ω turbulence models.

5.4.1. Moderate Dynamic Stall

When examining the coupled normal forces (Fig. 12) and pitching moments (Fig. 13) at the experimentally instrumented radial stations, the influence of aeroelastic coupling clearly reduces the impact of the aerodynamic differences observed in Figs. 6 and 7, respectively. The structural dynamic forces respond to the differences in aerodynamic forces by compensating in the deflection of the blade and the control angles. Both the normal force and pitching moments are almost coincident over the range of azimuth and radial stations. The most prominent difference is observed in Fig. 13(e). Both models predict a double moment stall just after 270°, but Menter k-ω SST uRANS model predicts a significantly larger magnitude for the second stall event than the Kok k-ω model. This magnitude difference is attributed to the addition of the SST correction, as Fig. 7(e) confirms that with prescribed motion that the SST correction increases the second stall event magnitude for the Kok k-ω model.

There are some significant differences observed between the OVERFLOW/RCAS results presented here when compared to the OVERFLOW/RCAS results in Grubb et al. (Ref. 16), even though the same mesh and numerical options were applied. While the exact turbulence model implementations evaluated here were not examined in Grubb et al., the consistency of all of the results, regardless of approach, particularly over the advancing rotor disk, indicates that the coupling here deviates, though the reason is currently not known at this time. However, even with these differences, as the simulations for the two turbulence models evaluated here were performed identically, relevant conclusions can be drawn.

The separation maps (Fig. 14) indicate that the influence of the two models over the rotor disk is more significant than indicated by the normal forces and moments. Compared with the original elsA/HOST Kok calculations performed by ONERA (Ref. 22), the separation maps are similar (Figs. 1(a) and 14(b)), even though the SST correction was not applied here. The extents of the FS1–FS3 regions are moderately smaller in the computations here, and the magnitudes tend to be larger, in particular in the fourth rotor quadrant. The Menter k-ω SST model here (Fig. 14(a)) indicates a slightly earlier and outboard extended start to region FS1, and the FS2 region is not captured. The FS3 region is also smaller than its Kok k-ω counterpart. The Menter k-ω SST model predicts an FS5 region, also observed in Grubb et al., while the FS5 region is absent from the Kok k-ω model predictions.

A final correlation can be made by examining the control angles resulting from the aeroelastic trim. The angle of the rotor disk, α_q as well as the collective angle of the blades θ_0, the lateral and longitudinal cyclic, θ_{1c}, θ_{1s} are all outcomes from the aeroelastic simulation. Table 4 presents the control angles from the original experiment and prior aeroelastic coupling analyses performed in Grubb et al. (Ref. 16), along with the predictions from these simulations.

Comparing the predicted angles from the two turbulence models in this study, the differences in the control angles occur in the second decimal place and are likely well within any measurement error for these angles. The observed differences in the coupling results between this work and Grubb et al. are seen in the cyclic angle predictions, as might be expected. There is minor to no change in the rotor shaft angle α_q predictions, which remain well below 5% when compared to experiment. Differences in the collective angle θ_0 remain within 0.2°-0.3° of the experimental value. The predictions here fall below the experimental value, while the prior predictions from Grubb et al. are above the experimental value. The cycle angle variations are approximately 0.5°-0.6°, but have much larger error values given the smaller angular values.

	α_q	θ_0	θ_{1c}	θ_{1s}
Experiment[1]	-6.7°	8.4°	3.16°	-3.51°
elaA/HOST[1] (Kok SST)	-6.46°	8.59°	3.3°	-3.69°
OVERFLOW/ RCAS[1] (Menter SST DDES)	-6.54°	8.81°	2.77°	-4.21°
Menter k-ω SST	-6.54°	8.19°	2.46°	-4.03°
Kok k-ω	-6.58°	8.14°	2.45°	-4.00°

Table 4: Trim control angles for 7A moderate dynamic stall trimmed aeroelastic analysis. [1]Results extracted from Grubb et al. (Ref. 16)

6. CONCLUSIONS

The Kok k-ω turbulence model, along with SST Corrections and DDES variants, has successfully been implemented in the OVERFLOW solver and validated for a series of two- and three-dimensional cases.

Based on the analyses performed, the following observations can be made:

- The Kok k-ω and Menter k-ω SST models provide similar aerodynamic results when flow is attached. Differences arise when the flow begins to separate. In particular the turbulent viscosity was observed to grow significantly in dynamic and separated cases for the Kok k-ω model, resulting in poor correlations. The problem is exacerbated for strong or large regions of separation and can result in numerical instabilities. The addition of the SST correction reduced this problem, but additional evaluation for aeroelastic rotors are still warranted.
- For prescribed motion simulations, the Kok and Menter uRANS results are largely identical for all variables examined. The predicted thrust coefficient varied by less than 1%. Minor variations were observed over small azimuth intervals of on the retreating side of the rotor disk, primarily beyond 80% of the blade radius. The extent and magnitude of the separation zones were mildly affected, with the largest difference observed in the prediction of the FS5 zone on the advancing side. The SST correction added to the Kok k-ω model reduced the observed differences between the models.
- The addition of DDES has minor impact on the aerodynamic blade loads and rotor loads with prescribed motion, for either for moderate or deep dynamic stall conditions.
- Coupled aeroelastic simulations of the rotor in moderate dynamic stall conditions reduces the minor differences observed in the prescribed motion cases. Thus, the aeroelastic coupling with the CSD solver compensates for at least some of the aerodynamic differences between the models. The largest differences occur near the rotor blade tip during pitching moment stall events. Integrated rotor values are within 1% for the two models evaluated. Some differences exist in the separation rotor maps, in particular for the fourth and first quadrants.

Current and planned studies are examining the cause of the differences in the coupling analyses with the prior cited work to understand the sensitivities given the same inputs for the study. In addition, the SST correction for the Kok k-ω model with DDES will be implemented and evaluated given the instabilities observed with the Kok k-ω model.

7. ACKNOWLEDGMENTS

This work was completed under Task 12 of the US-French International Partnership Agreement (IPA). The authors would like to acknowledge Rohit Jain and Arnaud Le Pape, the US and French leads of the IPA. Rohit Jain of the US Army, along with François Richez originally performed the simulations from which this investigation originated; both provided meshes, data, and guidance during this effort. The authors would particularly like to acknowledge the aid of Rohit Jain who provided invaluable help in performing the OVERFLOW-RCAS CFD-CSD coupling, without which this paper would have not been possible.

8. REFERENCES

[1] Biedron, R., and Lee-Rausch, E., “An Examination of Unsteady Airloads on a UH-60A Rotor: Computation Vs. Measurement,” Proceedings of the 68th Annual Vertical Flight Society Forum, May 1–3 2012.

[2] Burgess, N., and Jain, R., “Effects of Numerical Methods on Static and Dynamic Stall Simulations,” Proceedings of the 5th Decennial AHS Aeromechanics Specialist Conference, January 2014.

[3] Ahaus, L., Makinen, S., Meadowcroft, T., Tadghighi, H., Sanksar, L., and Baeder, J., “Assessment of CFD/CSD Analytical Tools for Improved Rotor Loads,” Proceedings of the American Helicopter Society 71st Annual Forum, May 2015.

[4] Ortun, B., Potsdam, M., Yeo, H., and Van Truong, K., “Rotor Loads Prediction on the ONERA 7A Rotor Using Loose Fluid/Structure Coupling,” *Journal of the American Helicopter Society*, Vol. 62, (3), July 2017, pp. 1–13. DOI: 10.4050/JAHS.62.032005

[5] Wilbur, I., Moushegian, A., Smith, M. J., and Whitehouse, G., “UH-60A Rotor Analysis with an Accurate Dual-Formulation Hybrid Aeroelastic Methodology,” *Journal of Aircraft*, Vol. 57, (1), January/February 2019, pp. 113–127. DOI: 10.2514/1.C035467

[6] Grubb, A., Smith, M. J., and Jain, R., “Physics of BVI-Induced Dynamic Stall on Equivalent One-Bladed and Four-Bladed Rotors,” Proceedings of the 77th Vertical Flight Society Annual Forum, May 2021.

[7] Yeo, H., and Ormiston, R., "UH-60A Airloads Workshop—Setting the Stage for the Rotorcraft CFD/CSD Revolution, Part I: Background and Initial Success," *Journal of the American Helicopter Society*, Vol. 67, (2), 2022, pp. 17. DOI: 10.4050/JAHS.67.022010

[8] Yeo, H., and Ormiston, R., "UH-60A Airloads Workshop—Setting the Stage for the Rotorcraft CFD/CSD Revolution, Part II: Ongoing Progress, Impact, and Lessons Learned," *Journal of the American Helicopter Society*, Vol. 67, (2), 2022, pp. 16. DOI: 10.4050/JAHS.67.022011

[9] Smith, M. J., Lim, J. W., van der Wall, B. G., Baeder, J., Biedron, R. T., Boyd, J., D.D., Jayaraman, B., Jung, S., and Min, B.-Y., "The HART II International Workshop: An Assessment of the State-of-the-Art in CFD/CSD Prediction," *CEAS The Aeronautical Journal*, Vol. 4, (4), 2013, pp. 345–372. DOI: 10.1007/s13272-013-0078-8

[10] Smith, M. J., Gardner, A. D., Jain, R., Peters, D. A., and Richez, F., "Rotating Wing Dynamic Stall: State of the Art and Future Directions," Proceedings of the 76th Vertical Flight Society Annual Forum, May/October 2020.

[11] Fitzgibbon, T., Barakos, G., Woodgate, M., and Jimenez-Garcia, A., "Numerical Simulations of Various Rotor Designs in Hover and Forward Flight," AIAA SciTech, January 7–11 2019. DOI: 10.2514/6.2019-0287

[12] Jain, R., "CFD Turbulence Transition Models Validation for Rotors in Unsteady Axial and Forward-flight Conditions using CREATETM-AV Helios," Proceedings of the 77th Annual Vertical Flight Society Forum, May 10–14 2021. DOI: 10.4050/F-0077-2021-16722

[13] van der Wall, B. G., "Comprehensive Rotary-Wing Database for Code Validation: The HART II International Workshop," *The Aeronautical Journal*, Vol. 115, (163), 2011, pp. 91–102, erratum p. 220. DOI: 10.1017/S0001924000005662

[14] Norman, T., Shinoda, P., Peterson, R., and Datta, A., "Full-Scale Wind Tunnel Test of the UH-60A Airloads Rotor," Proceedings of the American Helicopter Society 67th Annual Forum, 5 2011.

[15] Beaumier, P., Costes, M., and Gaveriaux, R., "Comparison between FP3D Full Potential Calculations and S1 Modane," 19th Annual European Rotorcraft Forum, September 1993.

[16] Grubb, A., Castells, C., Jain, R., Richez, F., and Smith, M. J., "High Fidelity CFD Analyses of Dynamic Stall on a Four-Bladed Fully Articulated Rotor System," Proceedings of the 2018 AHS 74th Annual Forum, May 14-17 2018.

[17] Richez, F., Jain, R., Smith, M. J., Grubb, A., and Castells, C., "Validation and Analysis of Aeroelastic Simulations of the UH-60A Rotor from Pre- to Post-stall Flight Conditions," Proceedings of the 76th Vertical Flight Society Annual Forum, May/October 2020. DOI: /10.4050/F-0076-2020-16469

[18] Cambier, L., Heib, S., and Plot, S., "The Onera elsA CFD software: input from research and feedback from industry," *Mechanics amp; Industry*, Vol. 14, (3), 2013, pp. 159–174. DOI: 10.1051/meca/2013056

[19] Kok, J., "Resolving the Dependence on Freestream Values for the k-ω Turbulence Model," *AIAA Journal*, Vol. 38, (7), July 2000, pp. 1292–1295. DOI: 10.2514/2.1101

[20] Menter, F., "Two-Equation Eddy-Viscosity Turbulence Models for Engineering Applications," *AIAA Journal*, Vol. 32, (8), August 1994, pp. 1598–1605. DOI: 10.2514/3.12149

[21] Nichols, R., and Buning, P., "User's Manual for OVERFLOW 2.3," Technical report, NASA Langley Research Center, Hampton, VA, June 2020.

[22] Richez, F., "Numerical Analysis of Dynamic Stall for Different Helicopter Rotor Flight Conditions," Proceedings of the 76th Vertical Flight Society Annual Forum & Technology Display , May 2017.

[23] Castells, C., Richez, F., and Costes, M., "A Numerical Investigation of the Influence of the Blade Vortex Interaction on the Dynamic Stall Onset in Simplified Rotor Environment," *Journal of the American Helicopter Society*, Vol. 66, (3), 2021, pp. 1–13. DOI: 10.4050/JAHS.66.032001

[24] Wilcox, D., "Reassessment of the Scale-Determining Equation for Advanced Turbulence Models," *AIAA Journal*, Vol. 26, (11), November 1988, pp. 1299–1310. DOI: 10.2514/3.10041

[25] Wilcox, D., "Comparison of Two-Equation Turbulence Models for Boundary Layers with Pressure Gradient," *AIAA Journal*, Vol. 31, (8), August 1993, pp. 1414–1421. DOI: /10.2514/3.11790

[26] Menter, F., Kuntz, M., and Langtry, R., "Ten years of industrial experience with the SST turbulence model," *Heat and Mass Transfer*, Vol. 4, January 2003.

[27] Rumsey, C., Smith, B., and Huang, G., “Description of a Website Resource for Turbulence Modeling Verification and Validation,” 40th Fluid Dynamics Conference and Exhibit, June/July 2010. DOI: 10.2514/6.2010-4742

[28] Wilcox, D., “A Two-Equation Turbulence Model for Wall-Bounded and Free-Shear Flows,” AIAA Paper 93-2906, July 1993. DOI: 10.2514/6.1996-2057

[29] Spalart, P., Deck, S., Shur, M., Squires, K., Strelets, M., and Travin, A., “A new version of detached-eddy simulation, resistant to ambiguous grid densities,” *Theoretical and Computational Fluid Dynamics*, Vol. 20, May 2006, pp. 181–195. DOI: 10.1007/s00162-006-0015-0

[30] Nichols, R. H., and Buning, P. G., *User’s Manual for OVERFLOW 2.3*, NASA Langley Research Center, Hampton, VA, https://overflow.larc.nasa.gov/users-manual-for-overflow-2-3, March 2021.

[31] Bir, G. S., “Structural Dynamics Verification of Rotorcraft Comprehensive Analysis System (RCAS),” Technical Report NREL/TP-500-35328, NREL, February 2005.

[32] Lopes, L. V., and Burley, C. L., “ANOPP2 User’s Manual,” Technical Report NASA/TM-2016-219342, NASA Langley, October 2016.

[33] Wissink, A. M., Jude, D., Jayaraman, B., Roget, B., Lakshminarayan, V. K., Sitaraman, J., Bauer, A. C., Forsythe, J. R., and Trigg, R. D., “New Capabilities in CREATE-AV Helios Version 11,” AIAA Scitech 2021 Forum, Virtual, January 2021. DOI: 10.2514/6.2021-0235

[34] Coles, D., and Wadcock, A. J., “Flying-Hot-wire Study of Flow Past an NACA 4412 Airfoil at Maximum Lift,” *AIAA Journal*, Vol. 17, (4), 1979, pp. 321–329. DOI: 10.2514/3.61127

[35] Ladson, C., “Effects of Independent Variation of Mach and Reynolds Numbers on the Low-speed Aerodynamic Characteristic of the NACA 0012 Airfoil Section,” Technical Report 19880019495, NASA Langley Research Center, Hampton, VA, October 1988.

[36] Langtry, R., Sengupta, K., Yeh, D., and Dorgan, A., “Extending the γ-Re$_{\Theta t}$ Local Correlation based Transition Model for Crossflow Effects,” 45th AIAA Fluid Dynamics Conference, June 2015. DOI: 10.2514/6.2015-2474

[37] Chan, W., “CAD Interface, Strand Grid Technology, and Other New Developments in Chimera Grid Tools 2.0,” Proceedings of the 8th Symposium on Overset Composite Grids and Solution Technology, October 2006.

[38] Saberi, H., Khoshlahjeh, M., Ormiston, R., and Rutkowski, M., “Overview of RCAS and application to advanced rotorcraft problems,” *AHS International 4th Decennial Specialists’ Conference on Aeromechanics*, January 2004, pp. 741–781.

[39] Wissink, A. M., Sitaraman, J., Jayaraman, B., Roget, B., Lakshminarayan, V. K., Potsdam, M. A., Jain, R., Bauer, A., and Strawn, R., “Recent Advancements in the Helios Rotorcraft Simulation Code,” 54th AIAA Aerospace Sciences Meeting, January 2016. DOI: 10.2514/6.2016-0563

[40] Leffell, J. I., Sitaraman, J., Lakshminarayan, V. K., and Wissink, A. M., “Towards Efficient Parallel-in-Time Simulation of Periodic Flows,” 54th AIAA Aerospace Sciences Meeting, January 2016. DOI: 10.2514/6.2016-0066

[41] Potsdam, M., Yeo, H., and Johnson, W., “Rotor Airloads Prediction Using Loose Aerodynamic/Structural Coupling,” *Journal of Aircraft*, Vol. 43, (3), 2006, pp. 732–742. DOI: 10.2514/1.14006

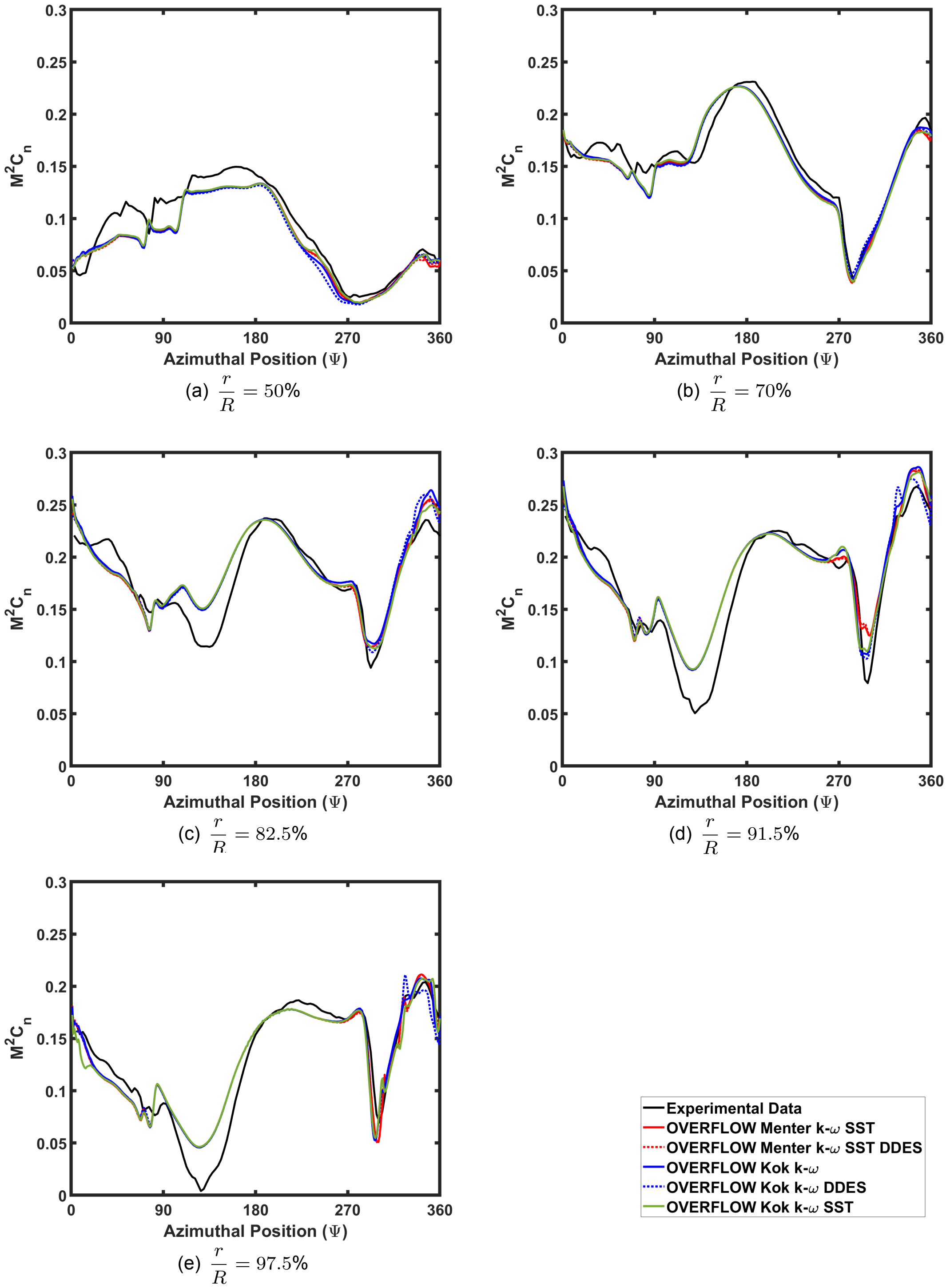

(a) $\frac{r}{R} = 50\%$

(b) $\frac{r}{R} = 70\%$

(c) $\frac{r}{R} = 82.5\%$

(d) $\frac{r}{R} = 91.5\%$

(e) $\frac{r}{R} = 97.5\%$

Figure 6: Azimuthal variation of the sectional normal force coefficient (C_n) at various radial stations for the moderate dynamic stall cases with prescribed aeroelastic motion

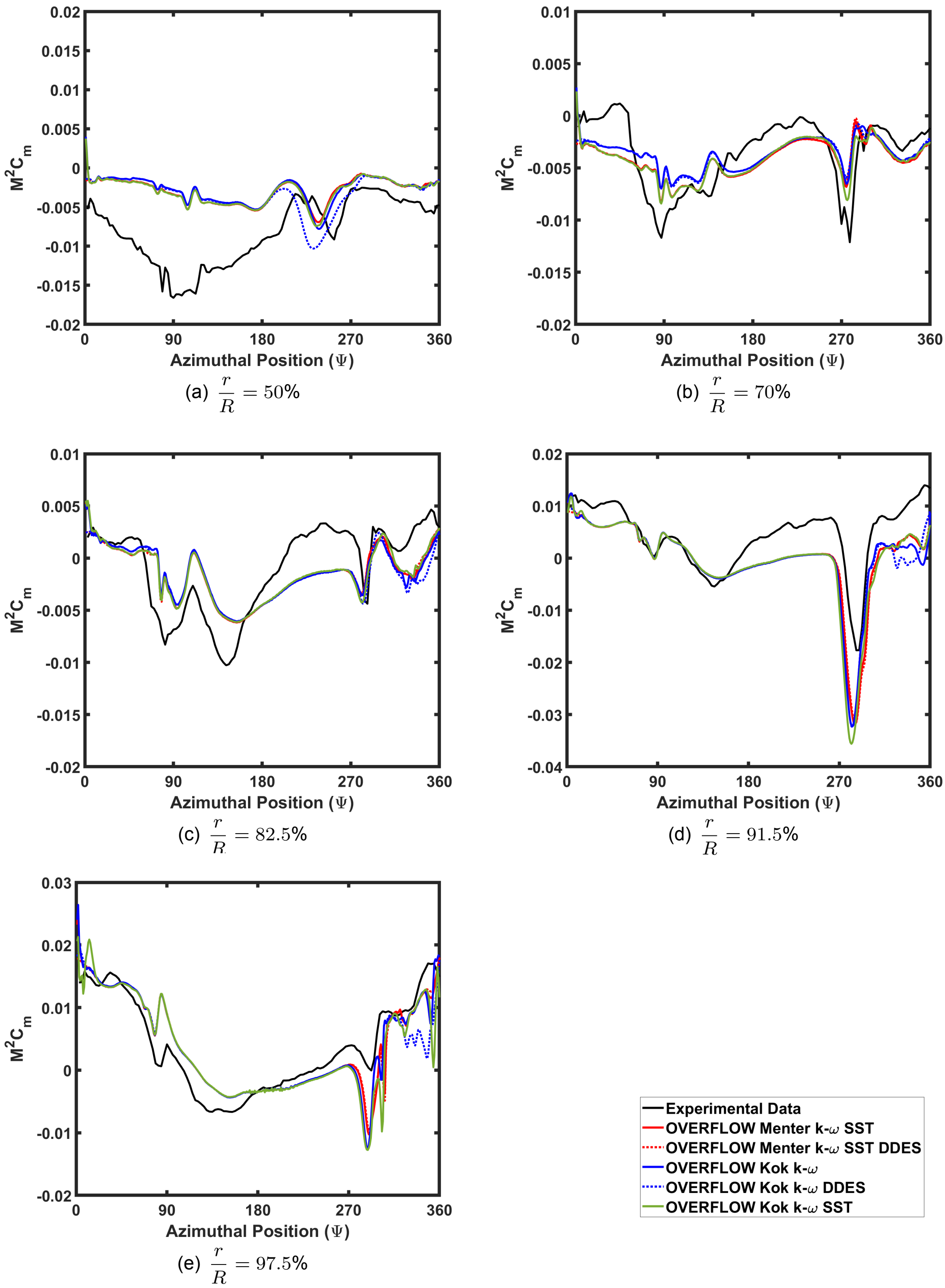

Figure 7: Azimuthal variation of the sectional pitching moment coefficient (C_m) at various radial stations for the moderate dynamic stall cases with prescribed aeroelastic motion

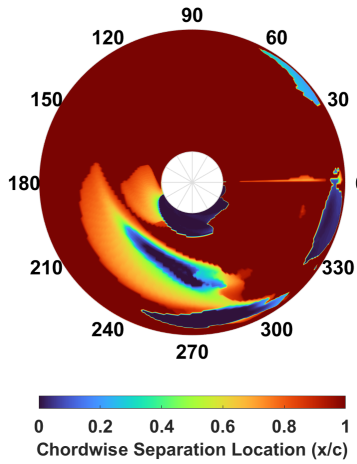

(a) Menter k-ω SST

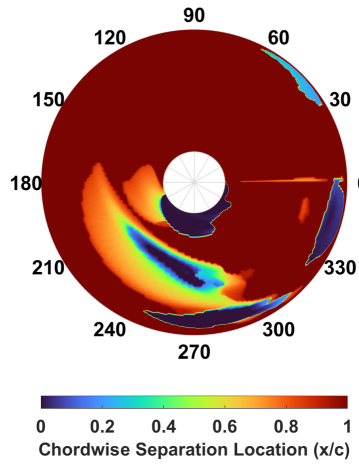

(b) Menter k-ω SST DDES

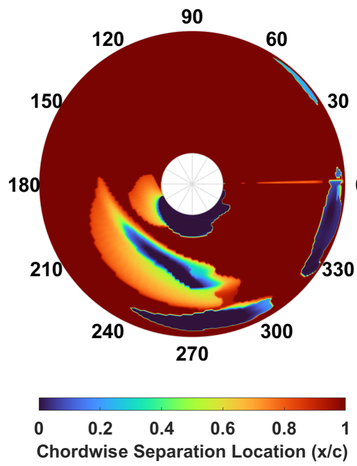

(c) Kok k-ω

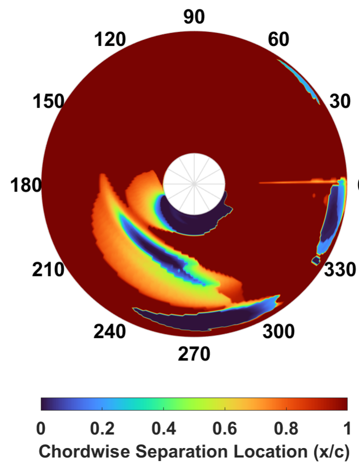

(d) Kok k-ω DDES

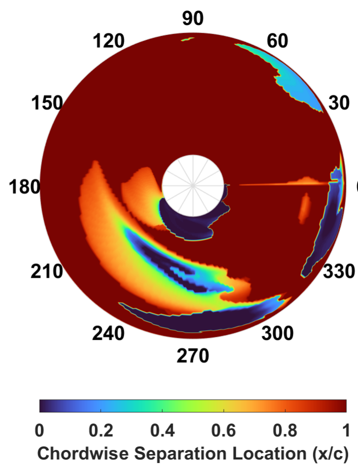

(e) Kok k-ω SST

Figure 8: Normalized flow separation location on the blade across the rotor disk for the moderate dynamic stall case with prescribed aeroelastic motion.

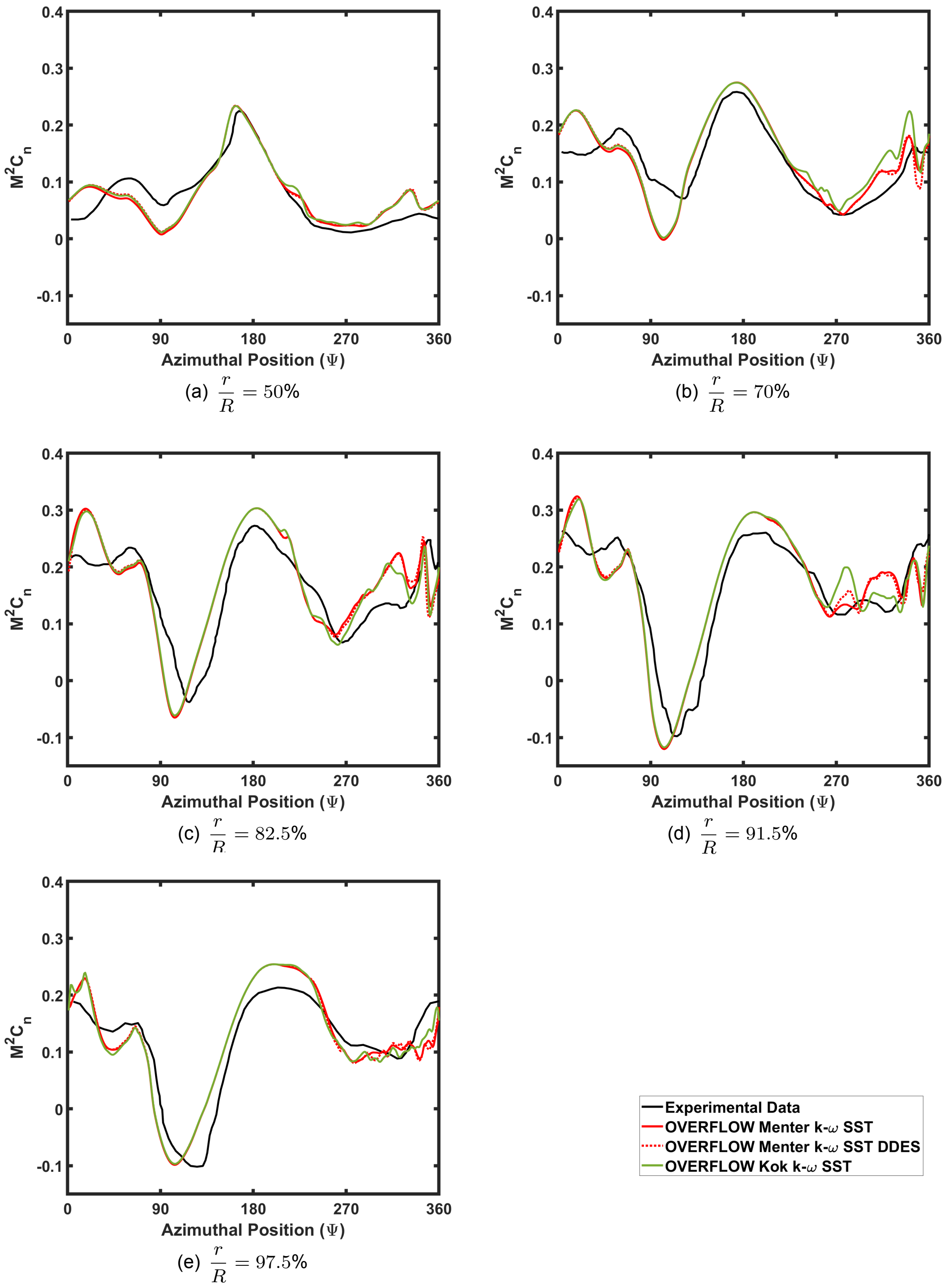

Figure 9: Azimuthal variation of the sectional normal force coefficient (C_n) at various radial stations for the deep dynamic stall cases with prescribed aeroelastic motion

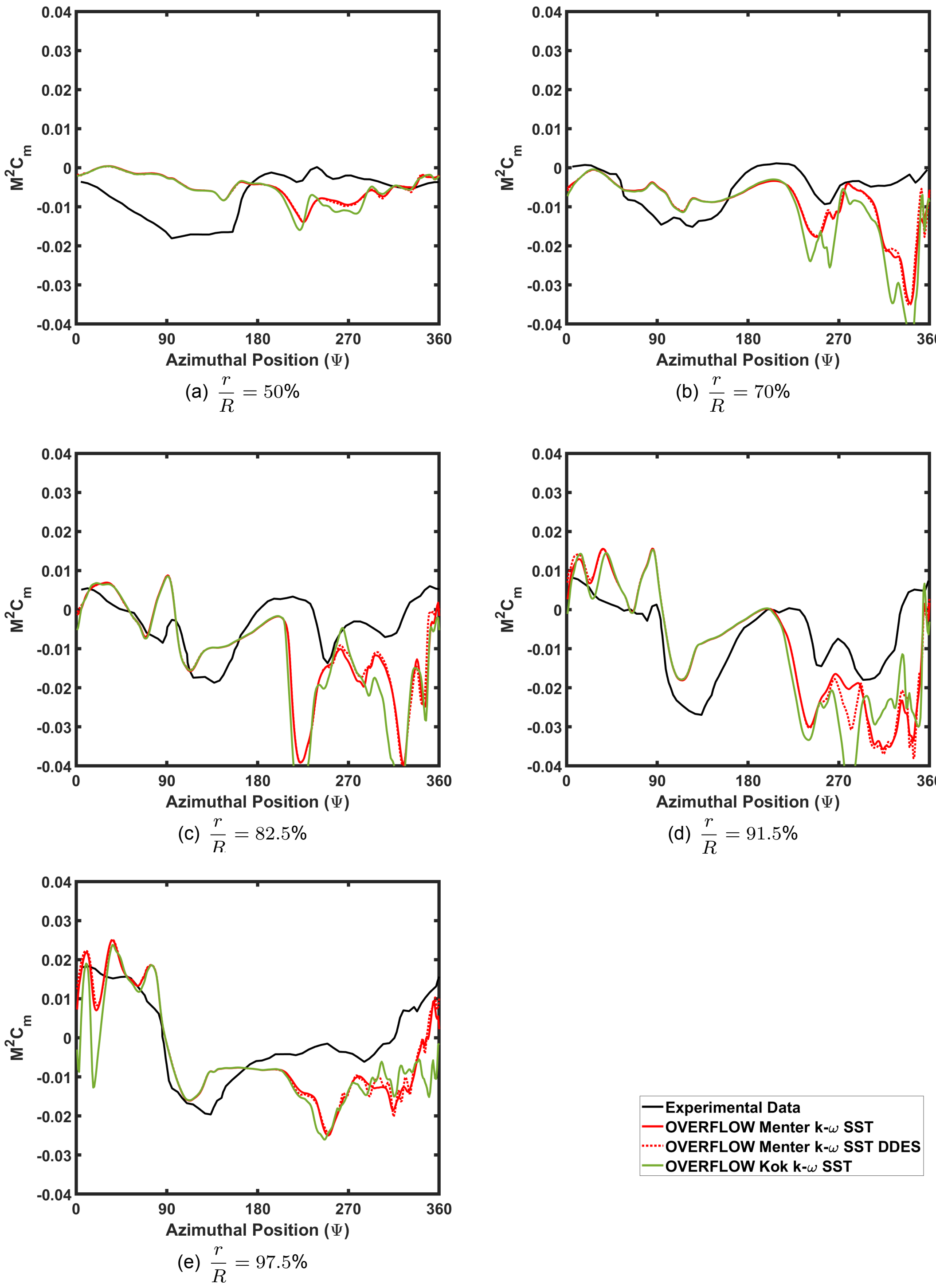

Figure 10: Azimuthal variation of the sectional pitching moment coefficient (C_m) at various radial stations for the deep dynamic stall cases with prescribed aeroelastic motion

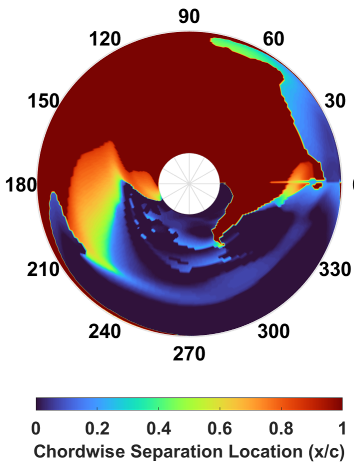

(a) Menter k-ω SST Model

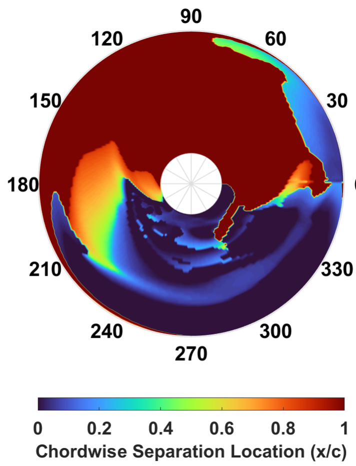

(b) Menter k-ω SST DDES Model

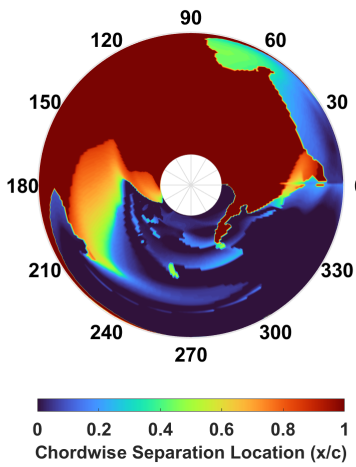

(c) Kok k-ω SST Model

Figure 11: Normalized flow separation location on the blade across the rotor disk for the deep dynamic stall case with prescribed aeroelastic motion

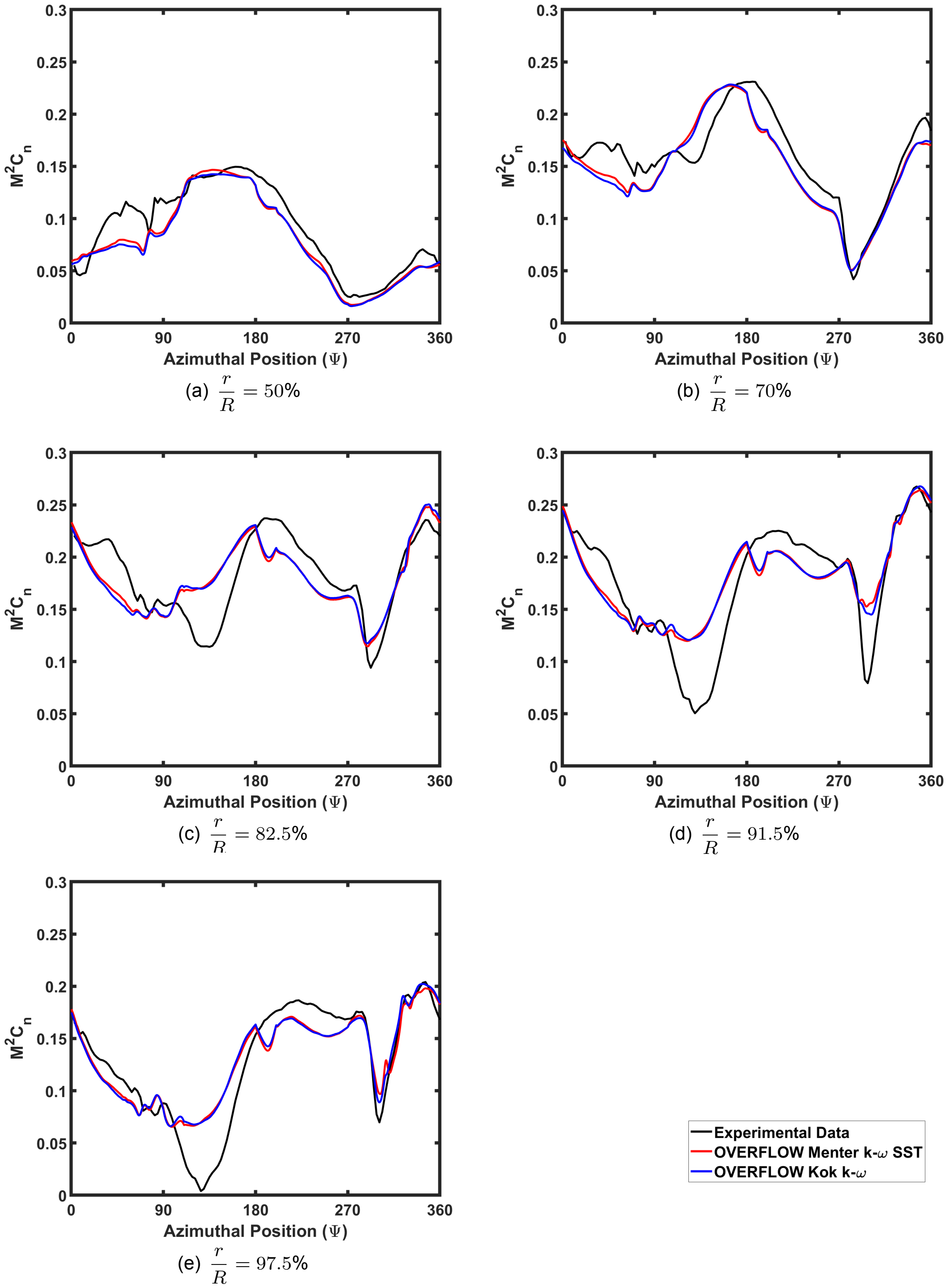

Figure 12: Azimuthal variation of the sectional normal force coefficient (C_n) at various radial stations for the moderate dynamic stall cases with CSD coupling

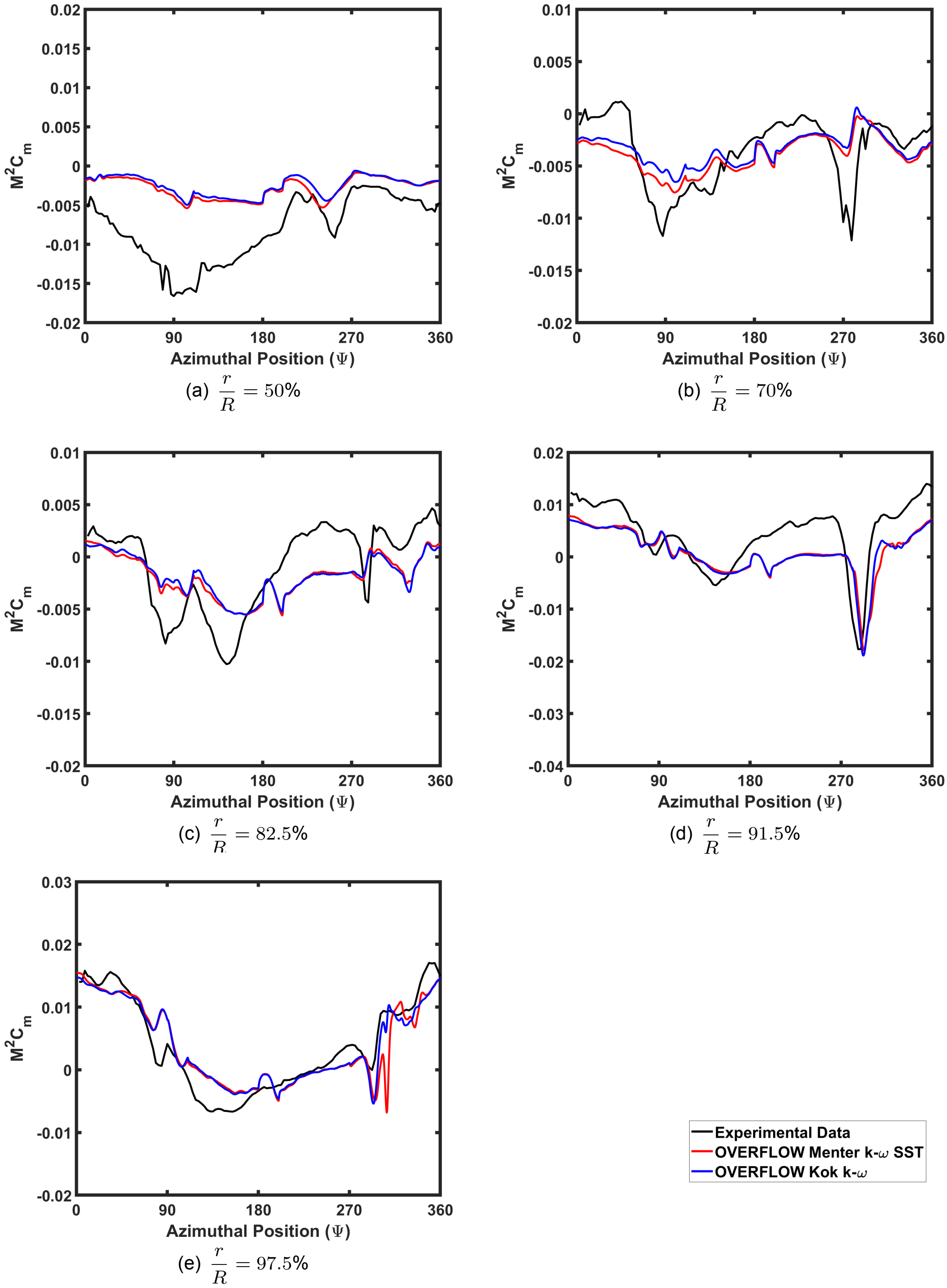

Figure 13: Azimuthal variation of the sectional pitching moment coefficient (C_m) at various radial stations for the moderate dynamic stall cases with CSD coupling

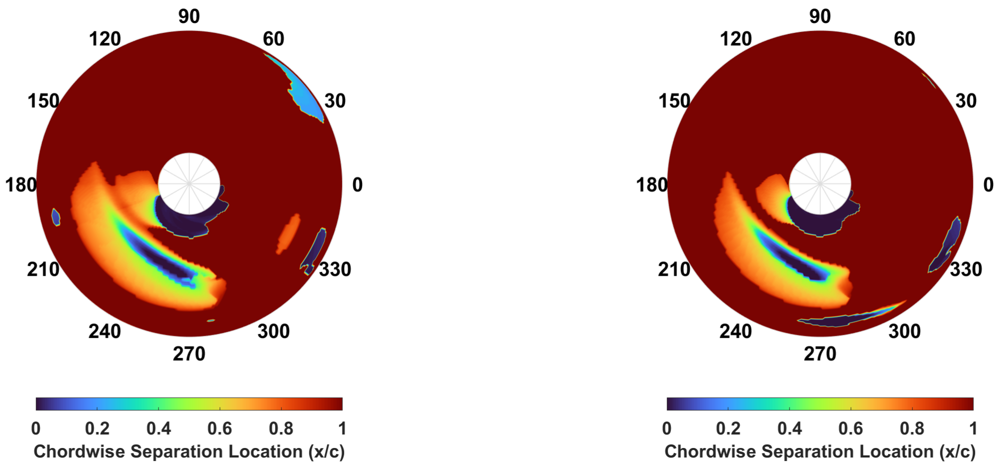

(a) Menter k-ω SST

(b) Kok k-ω

Figure 14: Normalized flow separation location on the blade across the rotor disk for the moderate dynamic stall case with CSD coupling.